Backward production in $\pi^- p \to p\pi^+\pi^-\pi^-$ at 8 GeV/c*

A. Abashian, B. Eisenstein, J. D. Hansen,† W. Mollet, G. R. Morris,‡ B. Nelson, T. O'Halloran, J. R. Orr,§ D. Rhines, P. Schultz,|| P. Sokolsky,¶ and R. G. Wagner
University of Illinois at Urbana-Champaign, Urbana, Illinois 61801

J. Watson
Argonne National Laboratory, Argonne, Illinois 60439

N. M. Gelfand
University of Chicago, Chicago, Illinois 60637
and University of Illinois at Urbana-Champaign, Urbana, Illinois 61801

M. Buttram
Iowa State University, Ames, Iowa 50010
(Received 21 July 1975)

We have studied backward baryon and meson production in $\pi^- p \to p\pi^+\pi^-\pi^-$ at 8.0 GeV/c using a streamer chamber triggered by the detection of a fast forward proton. Our data sample (1227 events) displays prominent $N^*\rho$ and N^*f quasi-two-body production. These states are investigated with regard to the peripheral nature of the production mechanism and sequential decay of the excited baryon and meson systems. The quasi-two-body production of $N^*\rho$ and N^*f intermediate states is consistent with u-channel proton exchange as the dominant production mechanism. In the $\pi^+\pi^-\pi^-$ mass distribution we observe a 3- to 4-standard-deviation enhancement at $M_{3\pi} = 1897 \pm 17$ MeV/c^2 with full width at half maximum $= 110 \pm 82$ MeV/c^2, but find no evidence for backward A_1 or A_2 production. We observe $\Delta^{++}(1232)$ production in the $p\pi^+$ effective mass distribution.

I. INTRODUCTION

At present only a few experimental studies of backward $\pi^- p$ inelastic processes have been conducted.[1] Cross sections for these backward processes are small compared to corresponding forward processes and, as a result, the acquisition of data is often very difficult. In an effort to understand the general features of the backward reaction

$$\pi^- p \to p\pi^+\pi^-\pi^- \quad (1)$$

we have performed an experiment using a Cherenkov-counter–hodoscope spectrometer to select events with a fast and forward proton (in the laboratory system) and a streamer chamber to detect the final-state particles.

The streamer-chamber trigger was designed to select an event sample characterized by very small momentum transfer u in the crossed channel and to maximize the acceptance for events with $600 < M(3\pi) < 2400$ MeV/c^2. As a result, the kinematic acceptance for backward resonance production involving two- and three-body baryon states is necessarily limited.

This experiment was the first to use the University of Illinois–ANL streamer-chamber facility[2] at Argonne National Laboratory. A total of 250 000 pictures were obtained. The film was scanned and events with four charged outgoing tracks were measured. Processing of the film measurements was accomplished using standard bubble-chamber programs modified to accommodate problems particular to streamer-chamber film. We report here the results of our investigation of 1227 events which gave a 4-constraint fit to reaction (1).

We find prominent $N^*\rho$ and N^*f quasi-two-body production. These states are discussed with emphasis on the peripheral nature of the production process and decay of the excited baryon and meson systems. In the 3π mass distribution we observe a 3- to 4-standard-deviation enhancement near 1900 MeV/c^2, but find no evidence for A_1 or A_2 production.

II. DATA ACQUISITION

An elevation view of the streamer-chamber spectrometer system is shown in Fig. 1. An 8.0-GeV/c π^- beam was focused on a liquid hydrogen target located inside the sensitive volume of the streamer chamber. The target consisted of a 3.8-cm-diameter by 30.5-cm-long liquid hydrogen flask enclosed in a foam vacuum box. The target position in the streamer chamber allowed 20 cm of entering beam track and about 80 cm of outgoing track to be viewed. The streamer chamber sensitive volume was 1.5 m × 1.0 m × 0.6 m. The chamber

was housed inside a large magnet with a 14.5 kG central field. The magnetic field was in the horizontal direction and bent negative beam particles down. Three cameras viewed the chamber in 18° stereo from a distance of about 2.0 m. Located downstream of the target and outside the region of the magnetic field was a 44.5-cm-diameter threshold Cherenkov counter filled with Freon 13 which was used to reject fast forward pions.

The streamer-chamber trigger required the interaction of a beam particle in the liquid hydrogen coupled with the detection of a fast forward proton candidate. A beam interaction in the hydrogen was defined by signals from a series of counters including B_3 upstream of the streamer-chamber magnet and no signal from counters B_4 or B_5. Counter B_4 was a rectangular counter with a 3.2-cm-diameter circular hole. It was positioned immediately upstream of the target vacuum box so that beam particles which passed through the hole would traverse the liquid hydrogen flask. Counter B_5 was centered on the deflected beam downstream of the streamer-chamber magnet.

Four counter hodoscopes were used to detect charged particles in the region of the Cherenkov counter. Two hodoscopes, H_2^h and H_3^h, each consisted of five horizontal scintillation elements, thus providing direction information in the vertical plane. The remaining hodoscopes, H_2^v and H_3^v, were each composed of three vertical elements. Signals from these hodoscopes were processed by a logic matrix and used with the Cherenkov counter in anticoincidence to define the fast forward proton part of the trigger.

Charged particles with low momenta which pass through the Cherenkov-counter–hodoscope system are characterized by the large angle the particle trajectories make with the Cherenkov-counter axis. The H_2-H_3 logic matrix was designed to make use of this information and eliminate from the trigger particles with momenta less than 3.0 GeV/c.

The Cherenkov counter was used as a veto in the trigger logic. Its pressure was maintained to give momentum thresholds for π's, K's, and p's of 1.25, 4.41, and 8.38 GeV/c, respectively.

The relationship between several useful kinematic parameters describing reaction (1) is shown in Fig. 2. The superscripts L and $*$ indicate quantities in the laboratory and center-of-mass systems, respectively, and θ_p is the scattering angle of the proton with respect to the beam direction. Plotted in this figure are contours of constant $M_{3\pi}$ and θ_p^* as a function of the proton laboratory mementum and laboratory scattering angle. The acceptance of the trigger proton by the Cherenkov-counter–hodoscope system limits the range of these variables that can be studied.

The geometrical acceptance of the trigger proton is governed by the solid angle subtended by the Cherenkov-counter–hodoscope system (~4.0 msr in lab) and also by the magnetic field surrounding the streamer chamber. For fixed production angles and vertex postion, a set of protons with varying momenta will have trajectories in the region of the Cherenkov-counter–hodoscope system which have been separated due to the presence of the magnetic field. The Cherenkov-counter–hodoscope system was positioned so that a proton produced 7.5 cm downstream of the center of the hydrogen flask with a recoil 3π mass of 1.3 GeV/c^2 and $\theta_p^* = 0°$ would pass through the cen-

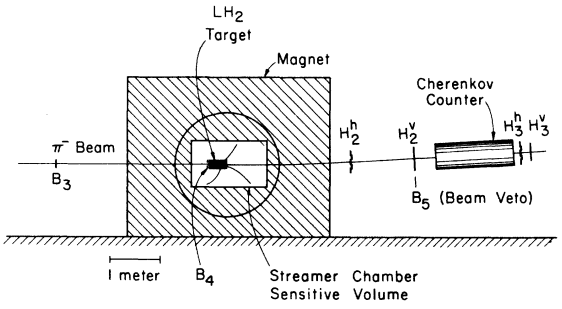

FIG. 1. Elevation view of streamer-chamber spectrometer system. B_3, B_4, and B_5 denote scintillation counters. H_2^h, H_2^v, H_3^h, and H_3^v are scintillation hodoscopes at each end of the proton-trigger Cherenkov counter.

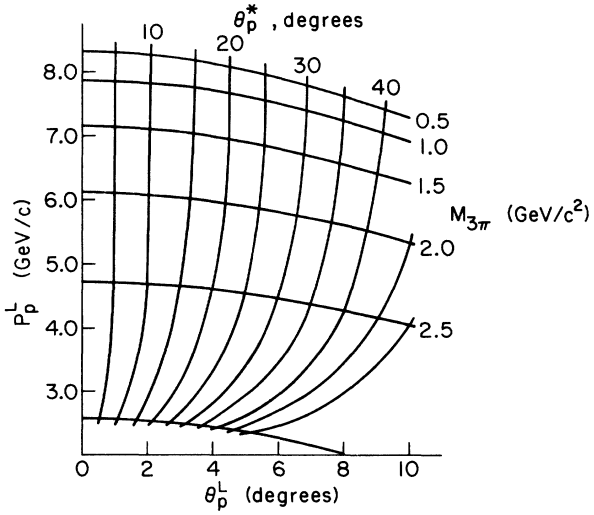

FIG. 2. Kinematic relationship between variables used to describe the backward reaction $\pi^- p \to p(3\pi)$. Contours of constant mass of the recoil 3π system and constant center-of-mass scattering angle of the outgoing proton are plotted for an incident beam momentum of 8.0 GeV/c.

tral axis of the Cherenkov counter.

Figure 3 shows the calculated geometrical acceptance of the trigger proton as a function of $M_{3\pi}$ and θ_p^L for the Cherenkov-counter position chosen for the data run. A constant beam direction and vertex position in the target have been assumed and each entry in the plot corresponds to ten times the calculated efficiency. This plot indicates that the efficiency for detecting the trigger proton is 1.0 for $600 \leq M_{3\pi} \leq 2400$ MeV/c^2 and $\theta_p^L \simeq 0°$. For small values of $M_{3\pi}$ (large proton momentum) the efficiency varies slowly between $\theta_p^L = 0°$ and $\theta_p^L \sim 2°$ ($\cos\theta_p^* \sim 0.98$). The efficiency falls rapidly to zero for larger angles. At the other extreme, for larger values of $M_{3\pi}$ (smaller proton momentum) the detection efficiency is zero for small θ_p^L and small, but nonzero, at larger angles.

The detection efficiency of the trigger proton is also a function of the beam direction and vertex position in the target. These parameters were taken into account in the Monte Carlo prescription used to make geometric efficiency corrections (see Appendix A).

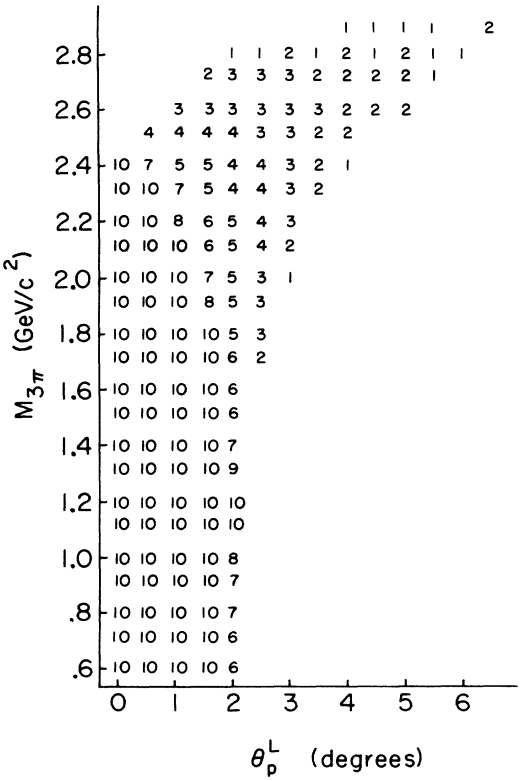

FIG. 3. Calculated geometrical acceptance of the trigger proton as a function of the recoil 3π mass and proton laboratory scattering angle. Each entry in the plot corresponds to ten times the calculated detection efficiency.

The target-full and target-empty trigger rates observed in the data run were 10.0 and $2.7/10^5$ π's incident on the liquid hydrogen target, respectively. The average beam flux on the hydrogen target was maintained near 2.0×10^4 π's/ZGS spill. The flux was limited by a 3-μsec streamer chamber memory time and a 600-msec ZGS spill coupled with the desire to minimize the number of extra beam tracks observed in a given event picture. An event rate of ~ 1.5 pictures/ZGS spill was obtained. This rate reflects a 200-msec streamer-chamber-system deadtime which was dominated by the time necessary to recharge the high-voltage system.

A total of 250 000 fast forward proton triggers were photographed which after deadtime corrections represent nearly 2.5×10^9 π's incident on the 30.5-cm-long liquid hydrogen target. In addition, 12 000 pictures triggered simply on interacting beam particles were obtained. This interacting beam data sample was used to check our procedure for determining a cross-section basis (see Appendix B).

III. DATA REDUCTION

The entire film sample was scanned twice. Much of the scanning was accomplished using an abbreviated set of scan rules designed to select charge balanced 4-prong events. However, about half of the film was scanned once using a detailed set of scanning instructions.

91% of the film was found to be scannable. Unscannable frames were typically either blank or too dim to be interpreted properly. About 80% of the scannable frames appeared to have an interaction vertex within the boundary of the foam target box. Many of the remaining triggers were due to beam particles which interacted downstream of the target (usually outside the sensitive volume of the streamer chamber) in such a manner that the Cherenkov-counter–hodoscope requirements were satisfied. Contamination was also observed from beam particle interactions upstream of the hydrogen target. A summary of scanning results is presented in Table I.

Nearly 51% of the scannable frames were observed to be charge-balanced single-vertex interactions. Those frames scanned as noncharge-balanced events were attributed to secondary interactions within the target and to tracks obscured by the foam target box or flaring. Table II displays how the charge-balanced single-vertex interactions were distributed between 2-, 4-, 6-, and 8-prong topologies. In particular, the 4-prong topology accounted for more than 25% of the scannable frames. The scanning efficiency

for finding 4-prong events in either of the two scans was 99.4%.

Nearly 34 000 4-prong interactions representing about two-thirds of the scanned 4-prong events were selected for measurement. Including remeasurements, 27 000 successfully measured events were obtained. Measurements were performed on DOLLY,[3] the University of Illinois automatic measuring machine. Normally, one-half of the outgoing tracks in a view were automatically measured. The remaining tracks were measured in an operator assisted mode. Tracks with special problems, e.g. too light or with large gaps, were digitized using a point measuring mode of operation. A measuring rate of 100 views (33 events) per hour was obtained for 4-prong events.

We used TVGP with a constant track setting error of 350 μ to perform the spatial reconstruction. TVGP was selected because it does not require knowledge of the primary vertex position, but reconstructs events on a track-by-track basis.

After spatial reconstruction, the University of Illinois routine VERTEX was used to reconstruct the primary vertex position. VERTEX extrapolates the outgoing tracks into the hydrogen target and determines the best vertex position by minimizing a χ^2 formed from the distances from the tracks to the proposed vertex weighted by appropriate errors. Contributions are included in track parameter errors to account for uncertainties due to Coulomb scattering in the target material and for the uncertainty in the determination of the vertex position. The distribution of the perpendicular distance from each track to the reconstructed vertex position for a sample of 4-prong events is shown in Fig. 4.

Kinematic fitting was performed using SQUAW. Due to problems in accurately digitizing the incoming beam track, nominal values were used. These nominal beam parameters and their errors were determined from measurement and subsequent spatial reconstruction of noninteracting beam tracks, investigation of test quantities calculated by SQUAW for 4C (4-constraint) fitted events, and the known dispersion of the beam. The values used were $p = 7.88 \pm 0.24$ GeV/c, $\phi = -24 \pm 10$ mrad, and $\lambda = 1.5 \pm 4.0$ mrad, where ϕ and λ are angles in the vertical and horizontal planes respectively and the values quoted are for the beam at the upstream end of the hydrogen flask.

TABLE I. Summary of scanning results.

Category	% of scannable frames
Target interaction with no observable vees or kinks	75.8
Target interaction + 1 vee	4.0
Target interaction + 2 vees	0.1
Target interaction + 1 vee and an associated kink	0.1
Beam track	12.1
Interaction not in target	4.2
Target interaction without a trigger candidate	2.7
Other	1.1

TABLE II. Fraction of scannable frames with charge balanced, even-prong topologies.

Topology	% of scannable frames
2-prong	14.0
4-prong	25.7
6-prong	9.9
8-prong	1.3

Cuts imposed on the event sample which gave a 4-constraint fit to reaction (1) included trigger proton momentum greater than 3.0 GeV/c, vertex reconstructed in the hydrogen flask, and a vertex χ^2 cut to eliminate events where a secondary track scattered or decayed. The kinematic χ^2 distribution for the resulting data sample is shown in Fig. 5. The smooth curve represents the expected distribution for four degrees of freedom plus a constant background. The data sample selected for analysis consisted of 1227 events with kinematic χ^2 less than 20.

We obtain fitted 2π and 3π effective mass errors in the ρ and A regions of ± 9 and ± 11 MeV/c^2 HWHM (half width at half maximum), respectively. To quantitatively check these error evaluations, we studied a sample of events which contain a visable

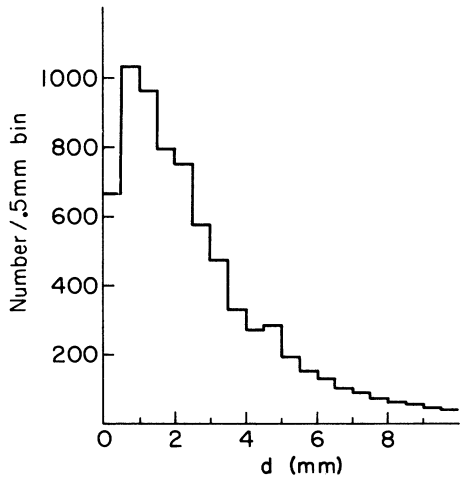

FIG. 4. Distribution of the distance of closest approach from all outgoing tracks to the reconstructed vertex position for a sample of 4-prong events.

vee. The events were measured and processed through SQUAW, where those events which gave a 1C fit to the hypothesis $K^\circ \to \pi^+\pi^-$ were selected. The measured errors for these K° events gave a mass resolution of ± 7 MeV/c^2 HWHM in reasonable agreement with the observed $\pi^+\pi^-$ effective mass distribution.

We convert numbers of events to cross sections using

$$\sigma = \sigma_b N ,$$

where N is the number of observed events corrected for losses due to the event acceptance of the streamer chamber spectrometer system and $\sigma_b = 0.88 \pm 0.11$ nb/event. σ_b includes corrections for scanning and measuring efficiencies, attenuation of the beam and secondary interactions within the target as well as factors to account for background contained in and good events eliminated from the selected event sample (see Appendix B).

IV. DATA ANALYSIS

A. General features

The most prominent features of the data can be seen in the triangle plot and mass projections shown in Fig. 6. The triangle plot consists of $p\pi_a^-$ and the corresponding recoil $\pi^+\pi_b^-$ effective masses. There are two entries per event. The $\pi^+\pi^-$ mass projection shows both ρ and f enhancements. A clear $\Delta(1232)$ signal is displayed in the $p\pi^-$ mass projection as well as a broad enhancement between 1450 and 1750 MeV/c^2. This broad enhancement appears from the triangle plot to be composed of resonances near 1520 and 1670 MeV/c^2. We associate events near 1520 MeV/c^2 with the $I=\frac{1}{2}$, $N(1520)$ as there are no established $I=\frac{3}{2}$ resonances near this mass. The 1670 enhancement could be due to either $I=\frac{1}{2}$ [$N(1670)$, $N(1688)$] or $I=\frac{3}{2}$ [$\Delta(1670)$] production. If the production is predominantly one-nucleon exchange, then the most reasonable composition of the enhancement based on comparison with low-energy πN scattering data is $I=\frac{1}{2}$ with $J=\frac{5}{2}$. We will refer to this enhancement as $N(1670)$.

There are suggestions of N^*, ρ, and f bands on the triangle plot corresponding to the quasi-three-body production of $N^*\pi^+\pi^-$, $p\pi^-\rho$, and $p\pi^- f$. However, a more prominent feature of the data, which we associate with quasi-two-body production, is the high concentration of events in regions where both N^* and ρ or f occur. Our analysis of these quasi-two-body $N^*\rho$ and $N^* f$ states will be presented in a later section.

In Fig. 7 we show the scatter plot of $M_{3\pi}$ and $\cos\theta^*$, where θ^* is the center-of-mass scattering angle of the 3π system with respect to the incoming beam direction. This scatter plot looks much as one would expect from studies of the trigger proton acceptance (see Fig. 3). A large fraction of the events is observed for $\cos\theta^* < -0.98$ and $M_{3\pi} \lesssim 2.4$ GeV/c^2.

Resonance production in the A region is not evident from the 3π mass projection of Fig. 7. However, we do observe an enhancement near 1900 MeV/c^2. Our analysis of the 3π final state has been reported in a previous communication.[4] In a later section, we will present more details of this analysis.

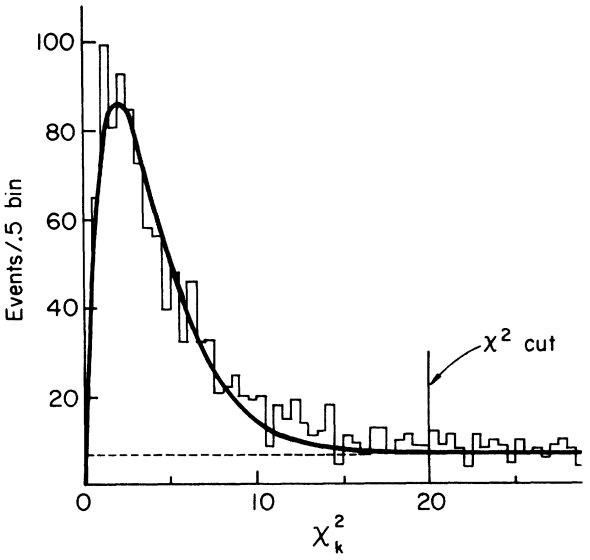

FIG. 5. Kinematic χ^2 distribution from 4-constraint fits. The curve represents the expected distribution plus a constant background.

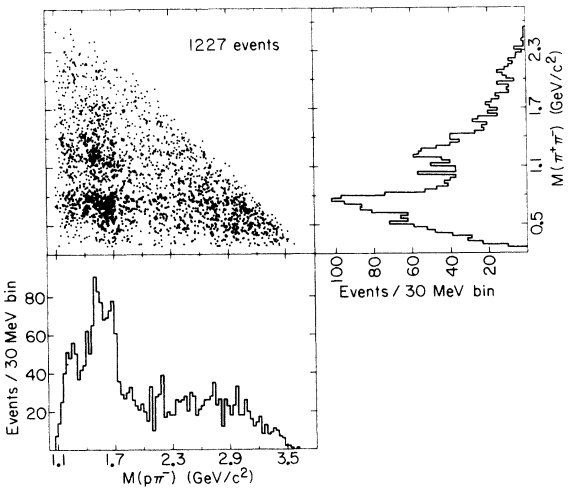

FIG. 6. Triangle plot of $p\pi_a^-$ and the corresponding recoil $\pi^+\pi_b^-$ effective masses (two entries per event).

The effective mass of the $p\pi^+$ system (see Fig. 8) shows some evidence for $\Delta^{++}(1232)$ production. The shaded distribution in Fig. 8 results from requiring $u' = u_{max} - u$ to be less than 0.5 $(\text{GeV}/c)^2$. Here, u is the 4-momentum transfer from the incident beam to the outgoing $p\pi^+$ system. Clearly, any $\Delta^{++}(1232)$ present in our data sample remains after making this u' cut.

Among the possible production mechanisms which could lead to $\Delta^{++}(1232)$ in our data sample are exotic ($I = \frac{5}{2}$) u-channel exchange coupling to the Δ^{++} at the beam vertex and $I = \frac{3}{2}$ u-channel exchange producing $p\pi^+\pi^-$ resonances which decay through the $\Delta^{++}\pi^-$ channel. Unfortunately, we are unable to draw conclusions from u distributions due to our limited acceptance for both the $p\pi^+$ and $p\pi^+\pi^-$ states.

$p\pi^+\pi^-$ effective mass distributions are shown in Fig. 9(a) for all events (two entries per event) and in Fig. 9(b) for events with $\cos\theta^*(p, p\pi^+\pi^-) < -0.9$. If both $p\pi^+\pi^-$ combinations satisfied this $\cos\theta^*$ cut, then only the combination with the smaller $\cos\theta^*$ was included in Fig. 9(b). The shaded distribution results from requiring the $p\pi^+$ effective mass to be in the 1232 region (1100–1360 MeV/c^2). Although an enhancement in these distributions is not apparent, most of the $\Delta^{++}\pi^-$ combinations shown in Fig. 9(b) have $p\pi^+\pi^-$ mass below 2.0 GeV/c^2. We have examined the $p\pi^+\pi^-$ effective mass as a function of $\cos\theta^*$ for $\Delta^{++}\pi^-$ combinations not shown in Fig. 9(b). No evidence of a $\Delta^{++}\pi^-$ enhancement was found.

For completeness, we show the $p\pi^-\pi^-$ effective mass distribution in Fig. 10 for all events and for events with $\cos\theta^*(p, p\pi^-\pi^-) < -0.9$. $I = \frac{1}{2}$ as well as $I = \frac{3}{2}$ u-channel exchange would be allowed for $p\pi^-\pi^-$ resonance production.

B. $N^*\rho$ and N^*f intermediate states

The triangle plot of the $p\pi^-$ and $\pi^+\pi^-$ systems (see Fig. 6) exhibits clear evidence for quasi-two-body baryon meson production. In this section we discuss these quasi-two-body processes with particular emphasis on the peripheralism of the production mechanism and the sequential decay of the intermediate baryon and meson systems.

The $p\pi^-$ mass projection is shown in Fig. 11(a) for those events with recoil $\pi^+\pi^-$ mass in the ρ

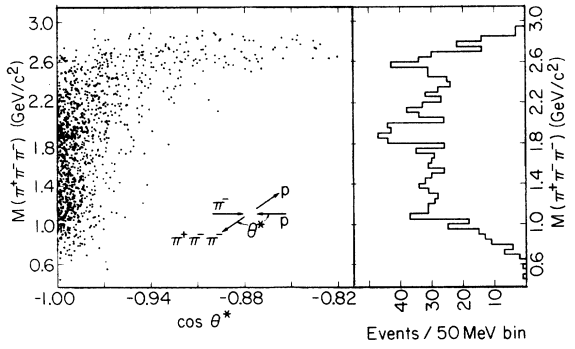

FIG. 7. Scatter plot of the 3π effective mass vs $\cos\theta^*$ for all 1227 events in our data sample.

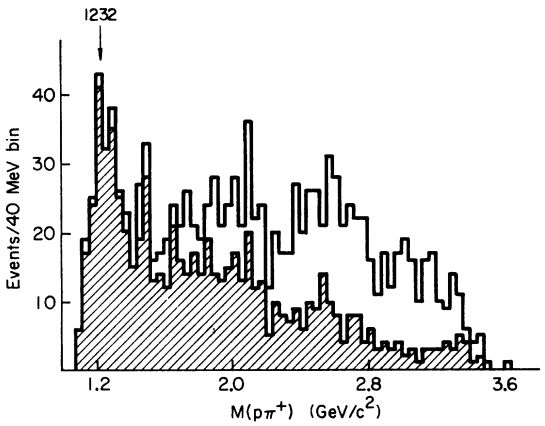

FIG. 8. $p\pi^+$ effective mass distribution. The shaded projection results from requiring $u' = u_{max} - u$ to be less than 0.5 $(\text{GeV}/c)^2$.

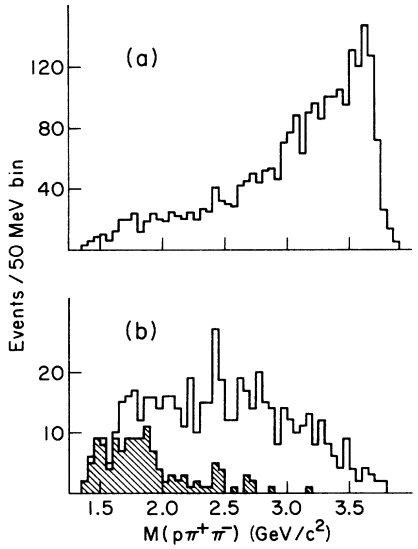

FIG. 9. $p\pi^+\pi^-$ effective mass distributions: (a) all events (two entries per event) and (b) events with $\cos\theta^*(p, p\pi^+\pi^-) < -0.9$ (more backward combination plotted). Shaded events result from requiring the $p\pi^+$ effective mass to be in the $\Delta^{++}(1232)$ region (1100–1360 MeV/c^2).

region (670–870 MeV/c^2). A rather small signal is observed for $\Delta(1232)$ production compared to the enhancements at 1520 and 1670 MeV/c^2. A similar observation can be made from Fig. 11(b), where the recoil $\pi^+\pi^-$ mass was chosen to be in the f region (1120–1420 MeV/c^2). However, in this case the enhancement near 1520 MeV/c^2 appears more pronounced that that near 1670 MeV/c^2.

In Fig. 12 we show $\pi^+\pi^-$ effective mass distributions for events with recoil $p\pi^-$ mass in the 1232 (1150–1350 MeV/c^2), 1520 (1425–1600 MeV/c^2), and 1670 (1600–1775 MeV/c^2) regions. These distributions exhibit small ρ and f signals for recoil opposite the $\Delta(1232)$, appreciable ρ and f production opposite the $N(1520)$, and a much stronger ρ than f signal for recoil opposite the 1670 baryon. Each of these distributions also exhibits a hint of an enhancement near 1.0 GeV/c^2. This region corresponds to the $I=0, S^*(993)$, but the statistical significance of these enhancements limits further consideration.

Due to the limited acceptance of our apparatus, we have had to use Monte Carlo techniques to gain insight into the nature of the production mechanisms for these quasi-two-body processes. Monte Carlo events were generated in accordance with a chosen model. An efficiency routine was employed to determine which of the generated events would have been detected in our apparatus. We

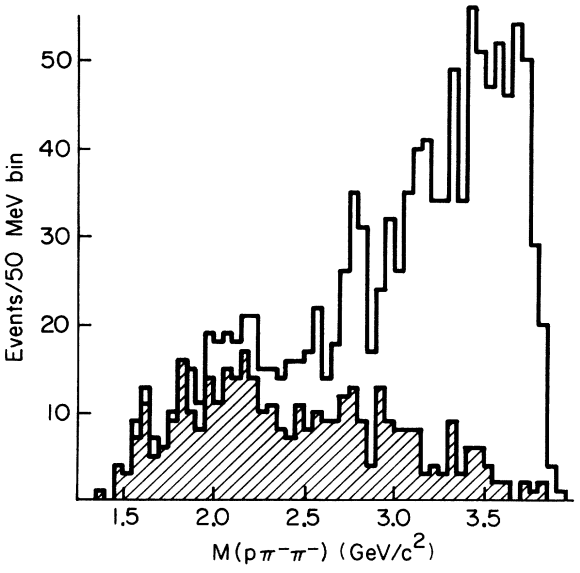

FIG. 10. $p\pi^-\pi^-$ effective mass distribution for all events and for events with $\cos\theta^*(p, p\pi^-\pi^-) < -0.9$ (shaded).

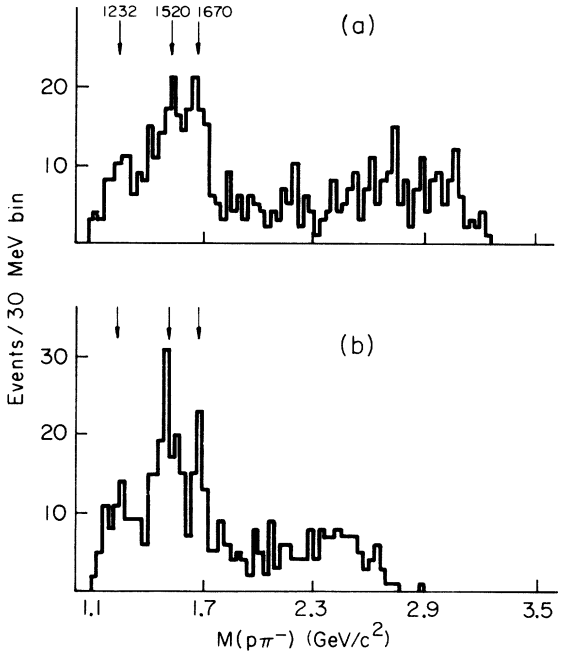

FIG. 11. $p\pi^-$ effective mass distributions for recoil $\pi^+\pi^-$ mass in (a) the ρ region (670–870 MeV/c^2) and (b) the f region (1120–1420 MeV/c^2).

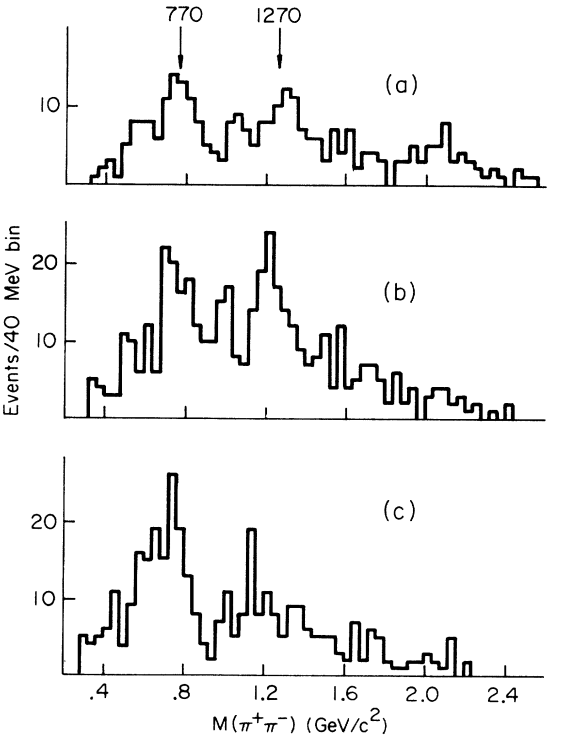

FIG. 12. $\pi^+\pi^-$ effective mass distributions for recoil $p\pi^-$ mass in (a) the 1232 region (1150–1350 MeV/c^2), (b) the 1520 region (1425–1600 MeV/c^2), and (c) the 1670 region (1600–1775 MeV/c^2).

were then able to make comparisons between distributions obtained from a detected Monte Carlo event sample and the observed data sample.

Figure 13 shows u' distributions for events from the data with $\pi^+\pi^-$ mass in the ρ or f region and recoil $p\pi^-$ mass in the 1232, 1520, or 1670 region. This figure also shows baryon decay angular distributions for these six states. The angles of the decay proton have been specified in the Gottfried-Jackson frame with the z axis in the direction of the incident pion and the y axis in the direction of the normal to the production plane.

u' and baryon decay angular distributions obtained from several Monte Carlo event samples are also shown in Fig. 13. Each of the Monte Carlo event samples was generated flat in u' and isotropic in ϕ^D. In addition, events were generated at several vertex positions within the target and with varying baryon mass within the limits of the mass region being considered. The ρ and f masses were fixed at 770 MeV/c^2 and 1270 MeV/c^2, respectively. Two or three event samples were generated for each of the six quasi-two-body states. These Monte Carlo event samples differed from each other only in the form chosen for the decay of the N^*. The detected Monte Carlo distributions have been normalized to the total number of observed events in each case.

Monte Carlo event samples for states involving the $\Delta(1232)$ and $N(1520)$ were generated according to the relation describing the decay of a spin-$\frac{3}{2}$ baryon into the $p\pi$ final state,

$$W_{3/2}(\theta^D) = \tfrac{1}{2}\rho_{11}(1+3\cos^2\theta^D) + \tfrac{3}{2}\rho_{33}\sin^2\theta^D ,$$

where $\rho_{11}+\rho_{33}=\frac{1}{2}$ and the notation $\rho_{2m,2m'}$ has been used for the baryon-spin-density-matrix elements. Monte Carlo event samples for states involving the 1670 baryon were generated according to the corresponding relation appropriate for a spin-$\frac{5}{2}$ state,

$$W_{5/2}(\theta^D) = \tfrac{3}{4}\rho_{11}(5\cos^4\theta^D - 2\cos^2\theta^D + 1) + \tfrac{3}{8}\rho_{33}\sin^2\theta^D(1+15\cos^2\theta^D) + \tfrac{15}{8}\rho_{55}\sin^4\theta^D ,$$

where $\rho_{11}+\rho_{33}+\rho_{55}=\frac{1}{2}$.

The best agreement between the observed baryon decay angular distributions and the detected Monte Carlo decay angular distributions occurs for the case where events were generated with only ρ_{11} nonzero. This is true for all six of the quasi-two-body states shown in Fig. 13. However, the possibility of diagonal matrix elements other than ρ_{11} being nonzero cannot be ruled out. In fact, all of the observed N^* decay angular distributions would be consistent with isotropic decay [$\rho_{11}=\rho_{33}=\frac{1}{4}$ for $\Delta(1232)$ and $N(1520)$; $\rho_{11}=\rho_{33}=\rho_{55}=\frac{1}{6}$ for $N(1670)$].[5]

For detected Monte Carlo event samples involving the $\Delta(1232)$ and $N(1520)$, the shape of the u' distribution does not change significantly with the decay of the baryon. For $N(1670)\rho$ and $N(1670)$ f states, the correlation between u' and $\cos\theta^D$ distributions is larger.

We show the detection efficiency in Fig. 14 for

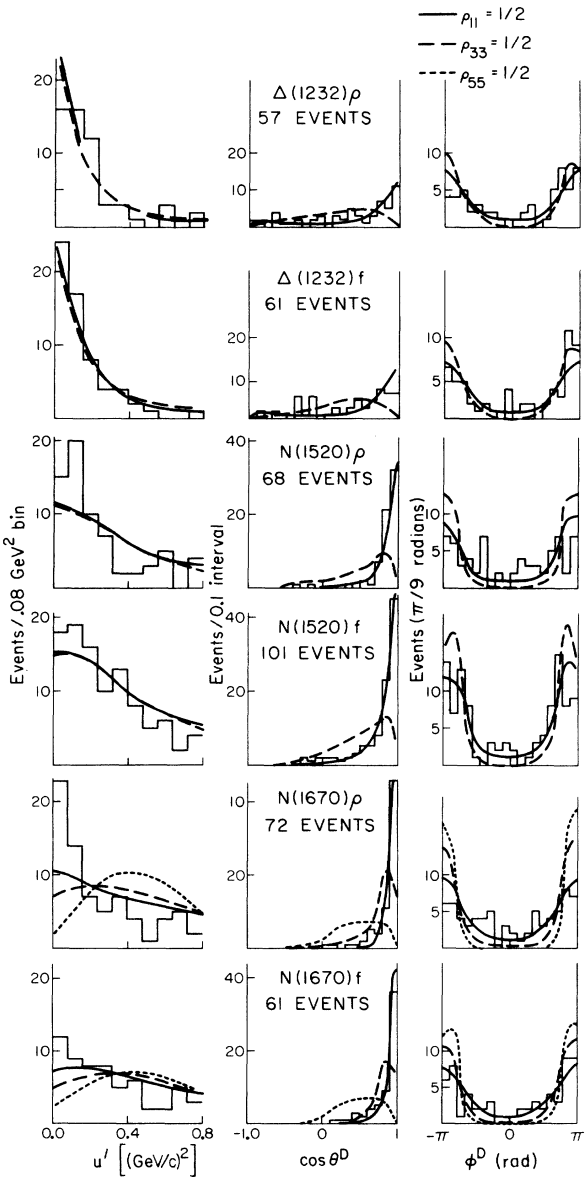

FIG. 13. u' and baryon decay angular distributions for the six quasi-two-body $N^*\rho$ and N^*f intermediate states. The angles of the decay proton are specified in the Gottfried-Jackson frame taking the direction of the incident beam as the z axis. The smooth curves represent detected Monte Carlo event samples all of which were generated flat in u' and isotropic in ϕ^D.

each of the Monte Carlo event samples generated. The over-all normalization clearly depends upon the decay distribution of the excited baryon. Moreover, if the spin-density-matrix elements vary appreciably with u', then corrections for our detection inefficiency should reflect this variation. Nevertheless, we have made corrections using the detection efficiencies shown in Fig. 14 for each of the six observed u' distributions. Figure 15 shows the resulting corrected u' distributions for the case where only ρ_{11} was assumed nonzero. Here, the errors reflect only the statistical uncertainties from the observed events. The solid lines represent fits to the form $dN/du' = Ae^{-Bu'}$. Listed in Table III are values and errors obtained for the slope parameter B, the total number of corrected events N_t, and the corresponding cross section for each of our parametrizations of the N^* decay. N_t was obtained by simply summing the corrected numbers of events for $u' < 0.8$ (GeV/c)^2, and the cross-section errors include our over-all normalization uncertainty as well as the statistical uncertainties.[6] We see evidence for backward peaking for $N(1520)\rho$ and $N(1670)\rho$ states.

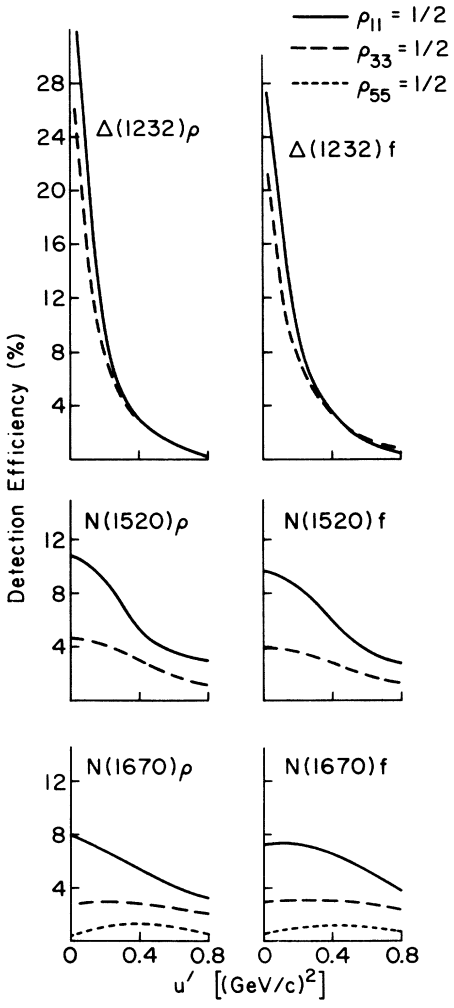

FIG. 14. Detection efficiency as a function of u' for each of our Monte Carlo event samples.

In Fig. 16 we display ρ and f decay angular distributions for recoil $p\pi^-$ mass in the 1232, 1520, and 1670 regions. The angles of the decay π^+ have been calculated in the Gottfried-Jackson frame with the z axis in the direction of the target proton. Decay angular distributions obtained from detected Monte Carlo event samples are also shown in these figures. Each of the event samples was generated flat in u' and with isotropic decay in the meson rest frame. In general, the detected distributions are nearly isotropic, indicating that acceptance corrections for observed distributions are relatively constant.

We obtain values for the spin-density-matrix elements of the ρ meson by fitting decay distributions using the relations

$$W_1(\cos\theta^D) = \tfrac{3}{4}[(1-\rho_{00}) + 3(\rho_{00}-1)\cos^2\theta^D],$$

$$W_1(\phi^D) = \frac{1}{2\pi}[1 + 2\rho_{1-1} - 4\rho_{1-1}\cos^2\phi^D],$$

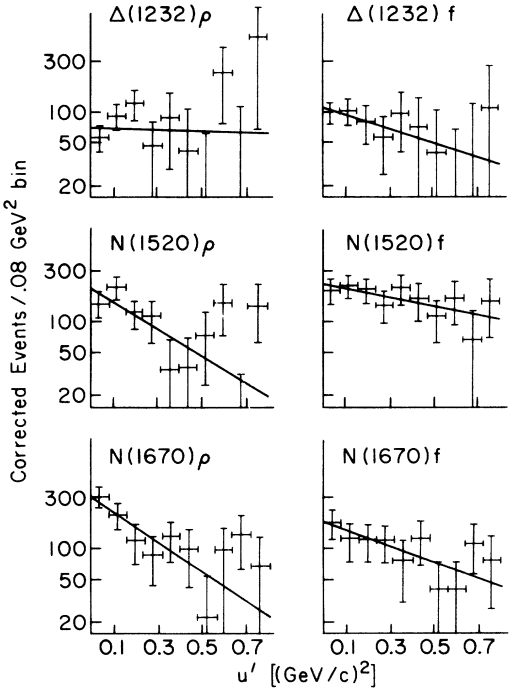

FIG. 15. Corrected u' distributions for the six N^*p and N^*f quasi-two-body states. Observed numbers of events were corrected using detection efficiencies resulting from only ρ_{11} being nonzero in our parametrization of the N^* decay.

TABLE III. Values obtained from quasi-two-body events for the slope parameter B [$dN/du' \propto e^{-Bu'}$, $u' < 0.8$ (GeV/c)^2], the total number of corrected events N_t, and the corresponding cross section for each of our parametrizations of the N^* decay.

State	Nonzero N^* decay matrix element	B [(GeV/c)$^{-2}$]	N_t	σ (μb)
$\Delta(1232)\rho$	ρ_{11}	0.2 ± 1.1	1120 ± 461	0.99 ± 0.43
	ρ_{33}	0.7 ± 1.1	918 ± 301	0.81 ± 0.28
$N(1520)\rho$	ρ_{11}	3.0 ± 0.9	972 ± 147	0.86 ± 0.17
	ρ_{33}	3.3 ± 0.9	2106 ± 322	1.85 ± 0.36
$N(1670)\rho$	ρ_{11}	3.3 ± 0.9	1208 ± 162	1.06 ± 0.19
	ρ_{33}	4.0 ± 1.0	2694 ± 344	2.37 ± 0.42
	ρ_{55}	9.3 ± 1.4	12 186 ± 1624	10.72 ± 1.94
$\Delta(1232)f$	ρ_{11}	1.6 ± 1.2	631 ± 227	0.56 ± 0.21
	ρ_{33}	2.0 ± 1.1	719 ± 233	0.63 ± 0.22
$N(1520)f$	ρ_{11}	1.0 ± 0.5	1567 ± 183	1.38 ± 0.23
	ρ_{33}	1.2 ± 0.6	3813 ± 445	3.36 ± 0.57
$N(1670)f$	ρ_{11}	1.7 ± 0.8	979 ± 141	0.86 ± 0.16
	ρ_{33}	2.3 ± 0.8	2142 ± 301	1.88 ± 0.35
	ρ_{55}	3.9 ± 0.9	7682 ± 1133	6.76 ± 1.30

and by calculating the moment $-\frac{5}{4}\sqrt{2}\,\langle \sin 2\theta^D \cos\phi^D \rangle$ to give $\mathrm{Re}\rho_{10}$. We have corrected for variations in acceptance with $\cos\theta^D$ and ϕ^D using weights obtained from the detected and isotropically generated Monte Carlo event samples. Our errors reflect only the statistical errors for the observed events. The resulting values for the spin-density matrix elements of the ρ are listed in Table IV.

The density-matrix elements we obtain for the ρ are consistent with the hypothesis that $\rho_{11} = \rho_{00} = \rho_{1-1} = \frac{1}{3}$ with all other matrix elements being zero. In addition, N^* decay distributions discussed previously are consistent with $\rho_{11} = \rho_{-1-1} = \frac{1}{2}$ with other diagonal matrix elements equal to zero. Both $I = \frac{1}{2}$ and $I = \frac{3}{2}$ u-channel exchange is allowed for backward $N^*\rho$ production. However, our matrix elements are consistent with the simpler hypothesis of unpolarized proton exchange being the dominant production mechanism.

The $\cos\theta^D$ distribution for the $N(1520)f$ state shown in Fig. 16 is considerably asymmetric. Investigation of the events near $\cos\theta^D = 1$ reveals that many of them have a $p\pi^-\pi^-$ effective mass near 2150 MeV/c^2. If a $p\pi^-\pi^-$ resonance were produced with $\cos\theta^*(p, p\pi^-\pi^-) \sim -1$ and these events were to overlap with $N(1520)f$ events, then the $p\pi^-\pi^-$ state should reflect into the f decay distribution near $\cos\theta^D = 1$. Decay distributions for $N(1520)f$ events which do not have their $p\pi^-\pi^-$ effective mass between 1.95 and 2.35 GeV/c^2 are also shown in Fig. 16 (dotted distributions). This cut tends to make the $\cos\theta^D$ distribution symmetric and removes the excess of events near $\phi^D = 0$.

We parametrize the corrected decay angular distributions for the f using

$$W_2(\cos\theta^D) = \tfrac{15}{8}[3\rho_{00}(\cos^2\theta^D - \tfrac{1}{3})^2 + 4\rho_{11}\sin^2\theta^D\cos^2\theta^D + \rho_{22}\sin^4\theta^D]$$

and

$$W_2(\phi^D) = \frac{1}{2\pi}[1 - 2(\rho_{1-1} + (\tfrac{2}{3})^{1/2}\,\mathrm{Re}\rho_{20})\cos 2\phi^D + 2\rho_{2-2}\cos 4\phi^D].$$

The distributions with the previously described $p\pi^-\pi^-$ mass cut were used for the $N(1520)f$ events. Errors used in the fits again reflect only the statistical errors for the observed events. The resulting values for the spin-density-matrix elements are listed in Table V.

The negative ρ_{22} value obtained from $\Delta(1232)f$ events indicates that a pure spin-2 decay distribution does not adequately describe the data. This is not very surprising considering the amount of background which is probably present in the selected $\Delta(1232)f$ events. The $N(1670)f$ event sample would also be expected to contain a large fraction of background.

Only $I = \frac{1}{2}$ u-channel exchange is allowed for

TABLE IV. ρ-spin-density-matrix elements obtained from quasi-two-body $N^*\rho$ events.

State	ρ_{00}	ρ_{11}	ρ_{1-1}	$\mathrm{Re}\rho_{10}$
$\Delta(1232)\rho$	0.30 ± 0.08	0.35 ± 0.07	−0.32 ± 0.15	−0.03 ± 0.10
$N(1520)\rho$	0.23 ± 0.07	0.39 ± 0.06	−0.07 ± 0.18	0.24 ± 0.09
$N(1670)\rho$	0.27 ± 0.07	0.36 ± 0.06	−0.14 ± 0.17	0.10 ± 0.12

TABLE V. f-spin-density-matrix elements obtained from quasi-two-body N^*f events.

State	ρ_{00}	ρ_{11}	ρ_{22}	$\rho_{1-1}+(\frac{2}{3})^{1/2}\mathrm{Re}\rho_{20}$	ρ_{2-2}
$\Delta(1232)f$	1.13 ± 0.36	0.69 ± 0.10	-0.75 ± 0.25	-0.02 ± 0.10	-0.07 ± 0.09
$N(1520)f$	0.23 ± 0.23	0.24 ± 0.07	0.14 ± 0.16	-0.02 ± 0.10	-0.07 ± 0.09
$N(1670)f$	0.77 ± 0.31	0.55 ± 0.09	-0.43 ± 0.22	0.05 ± 0.10	-0.07 ± 0.11

backward N^*f production. If proton exchange is the dominant production mechanism, then all of the f-spin-density-matrix elements with m or m' equal to 2 will be zero. For the N^*, proton exchange would also predict $\rho_{11}=\rho_{-1-1}=\frac{1}{2}$ with other diagonal matrix elements zero. While these data are not conclusive, we feel that they are consistent with proton exchange being the dominant production mechanism.

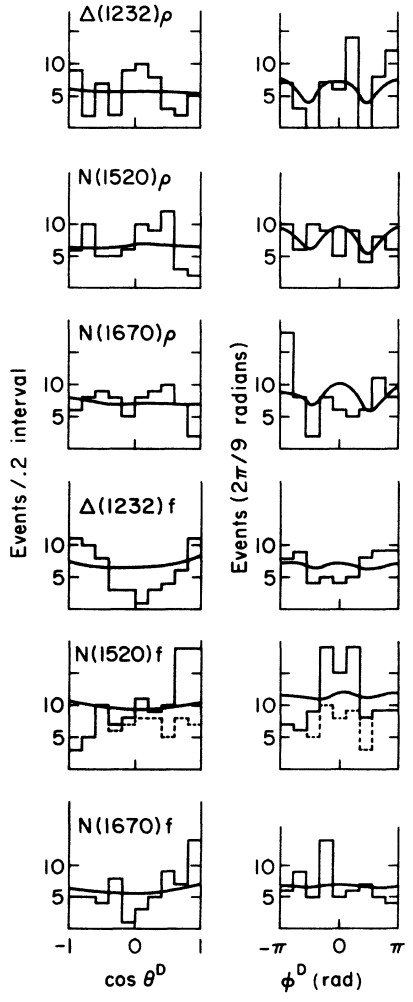

FIG. 16. ρ and f decay angular distributions for $N^*\rho$ and N^*f quasi-two-body states. The angles of the decay π^+ are specified in the Gottfried-Jackson frame taking the direction of the target proton as the z axis. The curves result from detected Monte Carlo event samples which were generated isotropic in $\cos(\theta^D)$ and ϕ^D.

We note that the $\pi^+\pi^-$ mass distribution for all events (see Fig. 6) appears to have an excess of events on the low-mass side of the ρ. From our Monte Carlo analysis, we have found that this effect is due to nonresonating $\pi^+\pi^-$ combinations associated with $N^*\rho$ quasi-two-body events.

C. The three-pion final state

The detection efficiency decreases smoothly and slowly with $\cos\theta^*(\pi_b^-, 3\pi)$ out to about -0.98 and is almost independent of $M_{3\pi}$ for mass values less than 2.2 GeV/c^2. For events with $M_{3\pi} < 2.2$ GeV/c^2 and $\cos\theta^* > -0.98$ the efficiency rapidly becomes small as the acceptance falls to zero. Nearly all of the events with large weights can be eliminated by requiring $\cos\theta^* < -0.98$.

Figure 17(a) shows the effective mass of the $\pi^+\pi^-\pi^-$ system weighted and unweighted for those events with $\cos\theta^* < -0.98$.[7] The general features of this distribution do not appear to be altered by correcting for the acceptance. The average weight, $\bar{\omega}$, for events in each 3π mass bin is shown in Fig. 17(b). $\bar{\omega}$ is essentially independent of $M_{3\pi}$ for mass values less than 2.2 GeV/c^2 and has a mean value of 3.07 over this mass region.

The most prominent feature in the 3π mass distribution is the enhancement near 1900 MeV/c^2. The solid curve shown in Fig. 18(a) is the result of a fit to a background[8] plus a Breit-Wigner modified by the background. The dotted line represents the background contribution in the 1900 region. This fit gives a 4-standard-deviation effect at $M_{3\pi} = 1897\pm17$ MeV/c^2 with a FWHM of 110 ± 82 MeV/c^2. Our fitted 3π mass resolution in the 1900 region is ±15 MeV/c^2. The number of observed events above background in the 3π mass interval from 1.8 to 2.0 GeV/c^2 is 53 ± 12. After corrections for acceptance, these events correspond to a cross section of 0.14 ± 0.04 μb.

The unshaded distributions shown in Figs. 18(b) and 18(c) contain events which had either $\pi^+\pi^-$ combination in the ρ region (670–870 MeV/c^2) or f region (1120–1420 MeV/c^2), respectively. The solid curves are the result of a fit to a simple background parametrization.[9] These distributions show no evidence for significant $\rho\pi$ or $f\pi$ decay

modes of the enhancement observed near 1900 MeV/c^2.

The shaded distributions in Figs. 18(b) and 18(c) show $\rho\pi$ and $f\pi$ mass distributions for those ρ or f combinations whose recoil $p\pi^-$ mass was in the N^* region (1425–1725 MeV/c^2). These distributions indicate that the enhancement observed near 1900 MeV/c^2 is not due to a reflection in the 3π mass distribution of $N^*\rho$ or N^*f events.

In an effort to better understand the background in the 1900 region, we show the 3π mass distribution for all quasi-two-body events in Fig. 19(a). Here, quasi-two-body events are defined as those with a $\pi^+\pi^-$ combination in the ρ or f region and with recoil $p\pi^-$ mass in the 1232, 1520, or 1670 region. Figure 19(b) displays the 3π mass distribution for those events which do not satisfy this quasi-two-body requirement.

We have obtained data over a very small interval in 4-momentum transfer as exhibited in Fig. 20. This figure displays $u' = u_{max} - u$ distributions for six 200 MeV/c^2-wide 3π mass intervals from the data sample with $\cos\theta^* < -0.98$. The shaded and unshaded distributions correspond to uncorrected and corrected numbers of events, respectively.

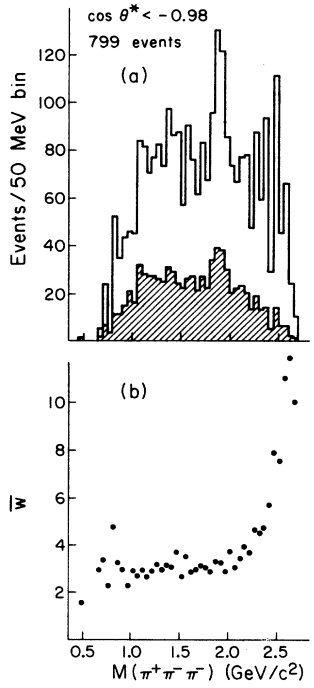

FIG. 17. (a) $\pi^+\pi^-\pi^-$ effective mass for events with $\cos\theta^*(\pi_b^-, \pi^+\pi^-\pi^-) < -0.98$. The shaded histogram shows the observed distribution. The unshaded histogram has been weighted on an event-by-event basis to correct for our event acceptance. (b) The average weight for each 50-MeV/c^2 mass interval.

For each of these distributions, the last u' bin containing events has been depleted due to the $\cos\theta^*$ cut. The error bars reflect only the statistical uncertainties from the observed events and thus should be regarded as lower limits since contributions to the error associated with weighting have not been included. We have fitted the u' distributions for events in the 1900 region using $dN_c/du' \propto e^{-Bu'}$ and obtain $B = 2.6 \pm 3.2$ (GeV/c)$^{-2}$.

We have investigated the Gottfried-Jackson decay angular distributions using the direction of the target proton as the z axis in the 3π rest frame. Both $\cos\theta^D$ and ϕ^D for all 3π mass intervals and

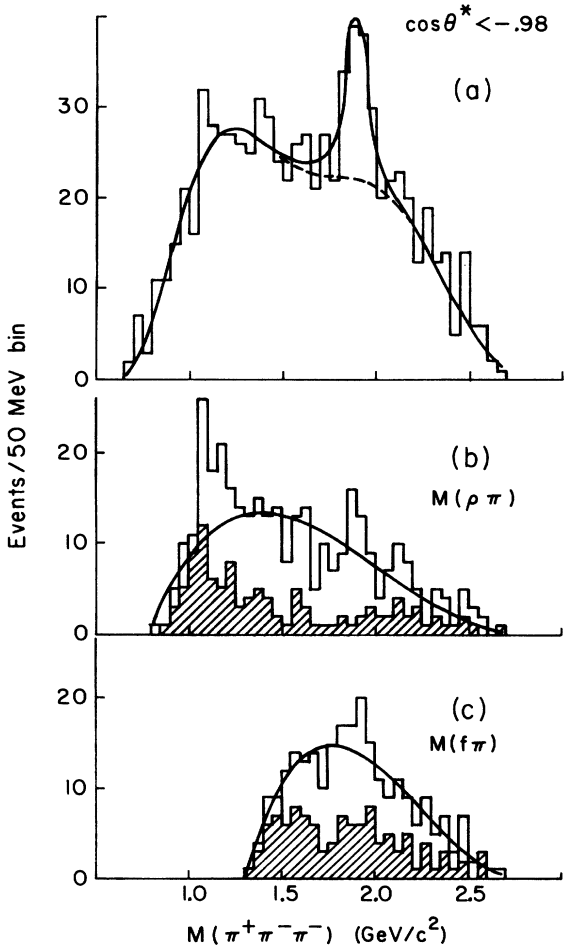

FIG. 18. Unweighted $\pi^+\pi^-\pi^-$ effective mass distributions for events with $\cos\theta^* < -0.98$. (a) All 799 events: The curve represents a background plus a Breit-Wigner distribution ($M_0 = 1897 \pm 17$ MeV/c^2, FWHM $= 110 \pm 82$ MeV/c^2) modified by the background. (b) and (c) contain events with either $\pi^+\pi^-$ combination in the ρ region (670–870 MeV/c^2) or f region (1120–1420 MeV/c^2), respectively. Shaded events are those with recoil $p\pi^-$ mass in the N^* region (1425–1725 MeV/c^2). The curves represent fits to a background parametrization.

in particular for the 1900-MeV/c^2 region are consistent with isotropy.

There is an indication in the $\rho\pi$ mass distribution of an enhancement in the A_1 region. However, the $\rho\pi$ mass distribution from $N^*\rho$ events also exhibits a peak in this region. We have investigated this feature by generating Monte Carlo $N(1670)\rho$ events as described in the preceding section using $\rho_{11} = \frac{1}{2}$ to parametrize the $N(1670)$ decay. Figure 21 shows detected Monte Carlo 3π mass distributions for events which were generated flat and peripheral ($d\sigma/du' \propto e^{-3.5u'}$) in u'. The peripheral events result in a $\rho\pi$ effective mass distribution which peaks in the A region, unlike events generated with a flat u' distribution.

Anderson *et al.*[1] have reported 100-MeV/c^2-wide enhancements at the A_1 and A_2 masses in a 16.0-GeV/c backward $\pi^- p$ missing-mass experiment. They also report less apparent effects at 8.0 GeV/c with total backward cross sections of $0.5^{+0.5}_{-0.3}$ μb for both A_1 and A_2 enhancements.

In order to place upper limits on resonance production in the A region, we have fitted the low-mass part of our observed 3π mass distribution to a smooth background parametrization plus 100-MeV/c^2-wide Breit-Wigner distributions at 1100 MeV/c^2 (A_1) and 1300 MeV/c^2 (A_2) modified by the background parametrization. This fit gives 27 ± 16 events for the A_1 and -13 ± 15 events for

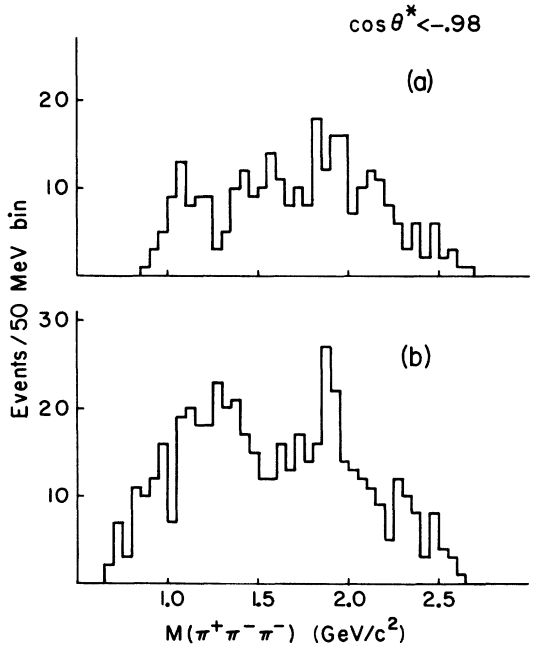

FIG. 19. Unweighted $\pi^+\pi^-\pi^-$ effective mass distributions: (a) Events with either $\pi^+\pi^-$ combination in the ρ or f region and with recoil $p\pi^-$ in the 1232, 1520, or 1670 region. (b) Events not included in (a).

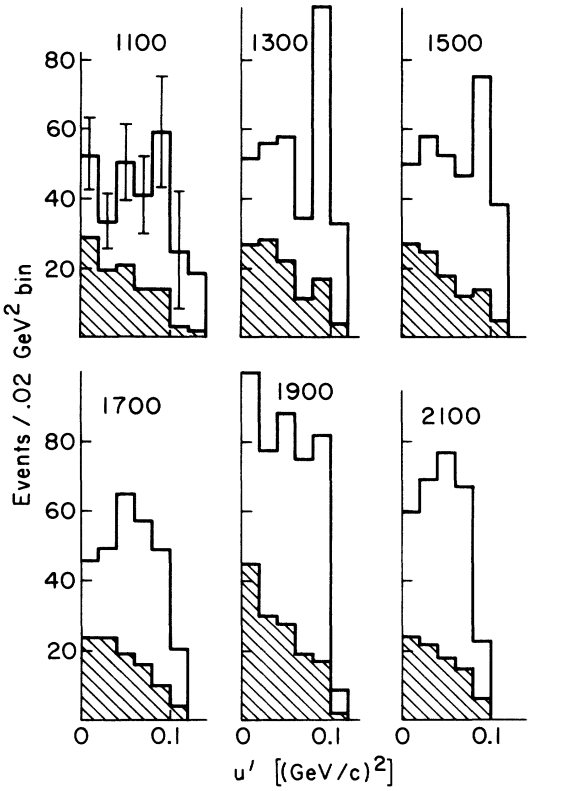

FIG. 20. $u' = u_{max} - u$ distributions for six 200-MeV/c^2-wide 3π mass intervals. The shaded and unshaded distributions correspond to observed and corrected numbers of events, respectively.

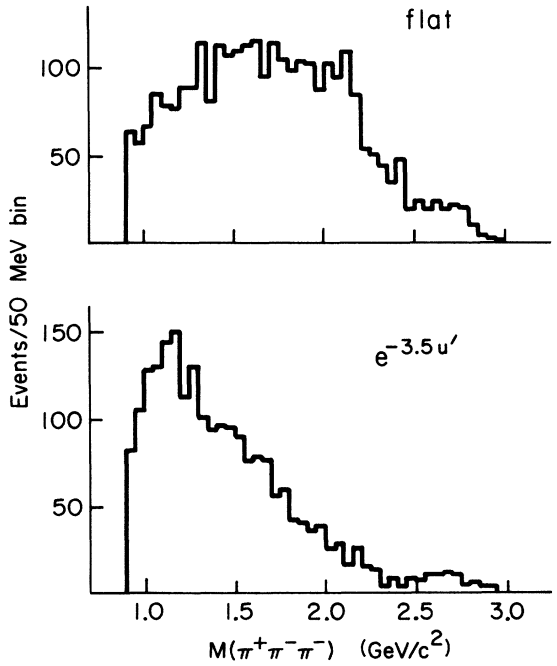

FIG. 21. 3π mass distributions from detected $N(1670)\rho$ Monte Carlo event samples.

the A_2 contribution to the 3π mass distribution. These numbers correspond to 95% C.L. (confidence level) cross-section upper limits of 0.159 μb and 0.081 μb for A_1 and A_2 production, respectively.

Our cross-section upper limits can be compared to the results of Anderson *et al.* if we correct for unobserved decay modes and use their assumption that $d\sigma/du \propto e^{-Bu}$ where $B = 3.16$ (GeV/c)$^{-2}$ as observed for backward elastic scattering at 8.0 GeV/c.[10] Using this prescription, we obtain $\sigma_{A_1}^{\text{tot}} < 0.95$ μb and $\sigma_{A_2}^{\text{tot}} < 0.70$ μb which are both lower than the 95% C.L. upper limits of 1.5 μb obtained from the results of Anderson *et al.* Removing ρN^* events (which tend to peak in the A_1 region) results in a lower upper limit for A_1 production of $\sigma_{A_1}^{\text{tot}} < 0.50$ μb.

V. SUMMARY AND COMMENTS

We observe quasi-two-body production of established resonant states in $N^*\rho$ and N^*f channels, but not in the $p(3\pi)$ channel. The production of $N^*\rho$ and N^*f states can proceed by $I = \frac{1}{2}$ u-channel exchange while a resonance decaying to 3 pions would require $I = \frac{3}{2}$ exchange alone. From this we infer that near $\cos\theta^* = 180^\circ$ $I = \frac{3}{2}$ exchange is suppressed relative to $I = \frac{1}{2}$ exchange.

We observe an enhancement with a statistical significance of 3 to 4 standard deviations near 1900 MeV/c^2 in the 3π mass spectrum. The large background under this enhancement is complicated and it is difficult to establish the nature of the effect. The effect corresponds to a cross section of ~ 0.14 μb [$u' < 0.1$ (GeV/c)^2], which is at least a factor of 2 smaller than the cross sections for $N^*\rho$ or N^*f production in an equivalent momentum transfer interval. We do not observe strong coupling to $\rho\pi$ or $f\pi$. This would suggest that experiments studying forward $\pi^- p \to (3\pi)p$, which could proceed by ρ or f t-channel exchange, might not observe this enhancement.

Our analysis of quasi-two-body $N^*\rho$ and N^*f channels is model-dependent. However, we are able to make some observations which are relatively insensitive to the assumptions of these models. The spin-density-matrix elements for the ρ and f mesons are consistent with u-channel proton exchange as the dominant production mechanism. We reach the same conclusion studying the decay of the N^*, but this conclusion is more dependent upon the details of our model. The differential cross sections for these quasi-two-body processes do not indicate structure (i.e., dips) similar to that observed in the backward charge exchange reaction $\pi^- p \to n\pi^0$.[11] We do see, however, that the differential cross sections for $N^*\rho$ states appear to have larger slopes than for N^*f states.

We find some evidence for $\Delta^{++}(1232)$ in our data sample. Production of this resonance would be of special interest if it were due to exotic ($I = \frac{5}{2}$) u-channel exchange. However, we are unable to make a definitive statement with regard to this production process, nor are we able to eliminate the possibility that $p\pi^+\pi^-$ resonances are produced which decay to $\Delta^{++}\pi^-$.

Finally, we mention the difficult problem of trying to interpret mass plots when competing channels are present. We have found that $N^*\rho$ quasi-two-body events accumulate in the 3π mass distribution near 1100 MeV/c^2. From this we see that any conclusions drawn from the 3π mass spectrum require an understanding of the background which in turn requires a complete kinematic analysis of the final-state particles.

ACKNOWLEDGMENTS

We would like to express our appreciation to B. Cork for his endorsement at a very early stage of development. We thank the Accelerator Research Facilities Division of Argonne National Laboratory, especially the streamer chamber crew. Many developments were possible only because of contributions from the Argonne engineering staff, in particular J. Dawson, R. Fuja, T. Kovarik, J. Peerson, and S. Prunster. We thank N. Beamer for his contributions with the experimental setup and A. Bross, who assisted with the data analysis. We are grateful for the labors of the scanning and measuring staff at the University of Illinois, and for the successful operation of DOLLY we thank R. M. Brown, R. Stamerjohn, and R. Gronek.

APPENDIX A: GEOMETRIC EFFICIENCY CORRECTIONS

Events which were not detected because of their geometric orientation with respect to the detection system were corrected for by weighting the observed events on an event-by-event basis.

In order to assign a weight to an observed event, a geometric detection efficiency for the event was calculated. Several Monte Carlo events were generated which differed from the observed event only in their orientation with respect to the detection apparatus. Monte Carlo variables described the azimuthal orientation of the event about the beam direction, the vertex position in the hydrogen flask, and the orientation of the beam direction at the vertex position.

By methods to be discussed in the following paragraphs, we assigned to each outgoing particle of a Monte Carlo event a probability for being detected in our apparatus. The probability for detecting each Monte Carlo event was obtained from

the product of the probabilities assigned for the detection of the outgoing tracks. For each observed event, the geometric detection efficiency was calculated by summing the probabilities obtained for the physically equivalent Monte Carlo events and dividing by the total number of Monte Carlo events generated.

The outgoing proton for each Monte Carlo event was extrapolated from the generated vertex position to the region of the Cherenkov counter-hodoscope system. The probability that the proton would have been detected was taken as 1.0 or 0.0 depending upon whether or not the proton trajectory satisfied the hodoscope logic requirements.

Two factors determined the probability assigned to the other outgoing Monte Carlo particles: (1) the probability that the track would not be lost because of the target vacuum box and (2) the probability that the track would not produce a flare.

A track which could be hidden by the target vacuum box was extrapolated to its intersection with the back plate of the streamer chamber. The probability that the track would not be lost was taken as 1.0 or 0.0 depending upon whether or not its intersection point was outside a rectangular region called the target shadow. The boundaries of the target shadow region were determined by requiring a minimum observable track length in all three views of 10 cm.

To study the effect of flaring, we chose from our observed events two samples of tracks which did not produce a proton trigger. One sample consisted of tracks within $\pm 10^\circ$ of the horizontal (xz) plane, the other of tracks within $\pm 10^\circ$ of the vertical (xy) plane (see Fig. 22). In each of these samples, we define ϕ as the angle between the track and beam direction. Azimuthal symmetry about the beam implies that the ϕ distributions of these two track samples should be the same. Figure 23 shows the ratio of the number of tracks near the horizontal plane (N_h) to the number of tracks near the vertical plane (N_v).

For ϕ greater than 70°, essentially all particles in the horizontal plane produce a flare and are not observed. For ϕ smaller than 45°, even though flaring does not occur, $N_h < N_v$ because the trigger proton has a tendency to be in the vertical plane and momentum conservation increases the probability of finding nontrigger particles in the same plane. We assume that the mechansim of flaring depends only upon the angle between the particle and electric field direction. The probability that a particle would not produce a flare was obtained using the solid line in Fig. 23 with $90^\circ - \phi$ as the angle between the particle and the direction of the electric field.

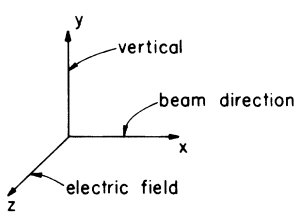

FIG. 22. Coordinate system used to study the effect of flaring.

APPENDIX B: CROSS-SECTION NORMALIZATION

Cross-section determinations were made using

$$\sigma = \sigma_b N ,$$

where N is the number of observed events corrected for losses due to the acceptance of the streamer-chamber spectrometer system and σ_b is the cross-section normalization. σ_b was determined from

$$\sigma_b = \frac{N_S^C \omega_1 \omega_2}{n N_m \epsilon} ,$$

where

N_S^C = the number of scanned 4-prong events corrected for scanning accuracy and losses,

N_m = the number of measured 4-prong events,

ϵ = the fraction of the data sample which was scannable,

ω_1 = a correction factor to account for the scattering of secondaries within the target,

ω_2 = a correction factor to account for events lost or gained in making cuts to select the 4C data sample,

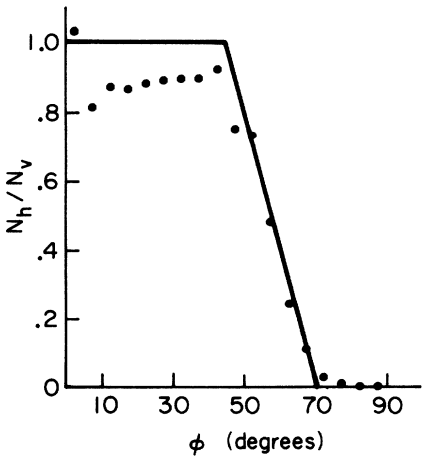

FIG. 23. Distribution of the ratio of the number of observed tracks in the horizontal and vertical planes. The electric field direction is in the horizontal plane at $\phi = 90^\circ$.

TABLE VI. Summary of factors used to obtain our cross-section normalization.

Quantity	Value
ρ (g/cm^3)	0.071 ± (1.0%)
l_e (cm)	30.0 ± (1.0%)
a_1	0.947 ± (0.4%)
a_2	0.940 ± (1.0%)
ϵ	0.901 ± (3.0%)
ω_1 [a]	1.087 ± (1.3%)
ω_2	0.92 ± (9.8%)
N_S^C for subsample	17720 ± (3.0%)
N_m for subsample	9663
$\bar{F}_{B_3/t}$ for subsample	9625
N_t for subsample	75741
σ_b for subsample (nb/event)	2.465 ± (10.9%)
number of 4C events from subsample	438 ± (4.8%)
number of 4C events from entire data sample	1227 ± (2.9%)
σ_b for entire data sample (nb/event)	0.880 ± (12.3%)

[a] This number includes a correction of (1.0 ± 0.5)% for knock-on electrons produced in the entrance window of the Cherenkov counter.

and n is the nb equivalent. The nb equivalent was determined from the total path length L using

$$n(\text{events/nb}) = \frac{A_0}{m_H} \rho L \times 10^{-33} ,$$

where A_0 = Avogadro's number, m_H = the atomic weight of hydrogen, and ρ = the hydrogen density (g/cm^3). The total path length of beam particles in the liquid hydrogen flask was obtained using

$$L = l_e \bar{F}_{B_3/t} N_t a_1 a_2 ,$$

where

l_e = the average length of liquid hydrogen traversed by noninteracting beam particles,

$F_{B_3/t}$ = the average beam flux recorded at counter $B3$ per streamer chamber trigger,

N_t = the number of triggers in the data sample,

a_1 = the beam attenuation between counter $B3$ and the downstream end of the hydrogen flask, and

a_2 = a correction factor to account for μ contamination in the beam.

The cross-section normalization was carefully determined for a subsample which amounted to slightly more than one-third of the total data sample. The corresponding cross-section normalization for the entire data sample was then obtained by scaling in proportion to the numbers of uncorrected 4-constraint events observed in the two samples. The cross-section normalization obtained for the entire data sample was 0.880 ± 0.108 nb/event. The factors which went into the determination of the cross-section normalization are listed in Table VI.

The cross-section normalization is composed of several factors which were obtained either indirectly from information recorded during the data run or inferred from physics principles. In order to check these methods, 2- and 4-prong topological cross sections were determined from a 12000-picture exposure triggered simply on interacting beam particles. The 2- and 4-prong topological cross sections obtained were 13.6 ± 1.4 mb and 10.1 ± 0.7 mb, respectively. These values are in good agreement with previously reported[12] values of 13.05 ± 0.05 mb for the 2-prong and 9.96 ± 0.07 mb for the 4-prong cross sections.

Our calculation of topological cross sections from these data differs in some respects from cross-section calculations using the trigger proton data sample. For the interacting beam particle data additional correction factors are necessary to account for interactions which did not produce a trigger because one of the secondaries struck counter B_5 (the beam veto) and to account for events where a slow proton did not have sufficient energy to escape from the target. In addition, topological cross-section determinations do not provide a check for our method of calculating the trigger proton's contribution to the event weight.

*Work supported in part by the U. S. Energy Research and Development Administration and the National Science Foundation.

†Present address: Niels Bohr Institute, Copenhagen, Denmark.

‡Present address: Enrico Fermi Institute, University of Chicago, Chicago, Ill.

§Present address: Fermi National Accelerator Laboratory, Batavia, Ill.

‖Present address: Argonne National Laboratory, Argonne, Ill.

¶Present address: Columbia University, New York, New York.

[1]Previous reports on backward $\pi^- p$ inelastic processes include P. B. Johnson *et al.*, Phys. Rev. 176, 1651 (1968); E. W. Anderson *et al.*, Phys. Rev. Lett. 22, 102 (1969); E. W. Anderson *et al.*, *ibid.* 22, 1390 (1969); J. P. Baton *et al.*, Nucl. Phys. B21, 551 (1970); S. Hagopian *et al.*, Phys. Rev. Lett. 24, 1445 (1970); J. E. Rice *et al.*, *ibid.* 27, 687 (1971); O. N. Baloshin *et al.*, Yad. Fiz. 14, 131 (1971) [Sov. Nucl. Phys. 14, 74 (1972)]; V. Vladimirskii *et al.*, Yad. Fiz. 17, 788 (1973) [Sov. Phys. 17, 411 (1973)].

[2]A. Abashian *et al.*, Nucl. Instrum. Meth. 115, 445 (1974).

[3]R. M. Brown and R. W. Downing, in *Proceedings of the International Conference on Advanced Data Processing for Bubble and Spark Chambers, Argonne National Laboratory 1968*, edited by R. J. Royston (Argonne National Laboratory, Argonne, Ill., 1968).

[4]A. Abashian *et al.*, Phys. Rev. Lett. 34, 691 (1975).

[5]Isotropic $\Delta(1232)$ decay would result in detected Monte Carlo distributions consisting of nearly equal ρ_{11} and ρ_{33} contributions, because the detection efficiency (see Fig. 14) is nearly equal for both components of the decay. Similarly, detected Monte Carlo distributions from isotropic $N(1520)$ or $N(1670)$ decay consist of large ρ_{11} contributions, since the detection efficiency is large for the ρ_{11} component relative to the other components.

[6]It should be pointed out that corrections for background contamination have not been made.

[7]In addition to the $\cos\theta^* < 0.98$ cut, a further requirement that the event weight be less than 20 was imposed to select the event sample analyzed in this section. This additional requirement eliminated 11 events, eight of which had $M_{3\pi} > 2.4$ GeV/c^2.

[8]The background has been parametrized by $(M-M_1)^{\alpha_1}(M_2-M)^{\alpha_2}(1+\beta_1 M+\beta_2 M^2)$, where M_1 and M_2 were fixed near the kinematic limits and α_1, α_2, β_1, and β_2 were parameters in the fit. Our fit gives $\alpha_1 = 3.60$, $\alpha_2 = 0.01$, $\beta_1 = -1.14$ (GeV/c^2)$^{-1}$, and $\beta_2 = 0.36$ (GeV/c^2)$^{-2}$.

[9]The background parametrization is $(M-M_1)^{\alpha_1}(M_2-M)^{\alpha_2}$. Our fit to the $\rho\pi$ mass distribution gives $\alpha_1 = 0.92$ and $\alpha_2 = 2.27$; to the $f\pi$ mass distribution $\alpha_1 = 1.04$ and $\alpha_2 = 2.34$.

[10]E. W. Anderson *et al.*, Phys. Rev. Lett. 20, 1529 (1968).

[11]J. P. Boright *et al.*, Phys. Lett. 33B, 615 (1970); R. C. Chase *et al.*, Phys. Rev. D 2, 2588 (1970).

[12]A. R. Dzierba *et al.*, Phys. Rev. D 2, 2544 (1970).